ACS NANO

www.acsnano.org

ARTICLE

Tailoring the Microstructure of Lamellar $Ti_3C_2T_x$ MXene Aerogel by Compressive Straining

Shelley D. Rawson,* Vildan Bayram, Samuel A. McDonald, Pei Yang, Loic Courtois, Yi Guo, Jiaqi Xu, Timothy L. Burnett, Suelen Barg, and Philip J. Withers

Cite This: *ACS Nano* 2022, 16, 1896–1908

Read Online

ACCESS | Metrics & More | Article Recommendations | Supporting Information

ABSTRACT: **Aerogels are attracting increasing interest due to their functional properties, such as lightweight and high porosity, which make them promising materials for energy storage and advanced composites. Compressive deformation allows the nano- and microstructure of lamellar freeze-cast aerogels to be tailored toward the aforementioned applications, where a 3D nanostructure of closely spaced, aligned sheets is desired. Quantitatively characterizing their microstructural evolution during compression is needed to allow optimization of manufacturing, understand in-service structural changes, and determine how aerogel structure relates to functional properties. Herein we have developed methods to quantitatively analyze lamellar aerogel domains, sheet spacing, and sheet orientation in 3D and to track their evolution as a function of increasing compression through synchrotron phase contrast X-ray microcomputed tomography (μCT). The as-cast domains are predominantly aligned with the freezing direction with random orientation in the orthogonal plane. Generally the sheets rotate toward flat and their spacing narrows progressively with increasing compression with negligible lateral strain (zero Poisson's ratio). This is with the exception of sheets close to parallel with the loading direction (Z), which maintain their orientation and sheet spacing until ~60% compression, beyond which they exhibit buckling. These data suggest that a single-domain, fully aligned as-cast aerogel is not necessary to produce a post-compression aligned lamellar structure and indicate how the spacing can be tailored as a function of compressive strain. The analysis methods presented herein are applicable to optimizing freeze-casting process and quantifying lamellar microdomain structures generally.**

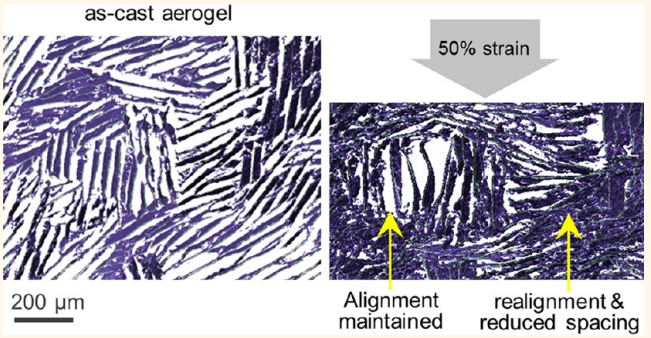

KEYWORDS: *freeze-casting, architectures, nanomaterial, micro domains, MXenes, time lapse imaging*

AEROGELS AND THEIR CHARACTERIZATION

Freeze-cast aerogels are an emerging class of materials exhibiting 3D architectures comprising sheets, tens of nanometers in thickness, within a 3D hierarchical structure. Control of the aerogel nano- and microstructure is key to tailoring them for high performance applications. Compression is a simple and effective way of modifying the sheet spacing and alignment.[1] Compressed aerogels are finding applications in an array of technologies including supercapacitors,[2] composites,[3] sensors,[4] and oil cleanup.[5] To precisely control their processing, methods for quantitatively analyzing and understanding the changes in aerogel architecture in three dimensions as a function of compression are needed which is the focus of this paper.

Aerogel manufacture via freeze-casting involves applying a temperature gradient to induce unidirectional freezing of a colloid, which causes the solid phase to be rejected by the growing ice crystals to the last to solidify interdendritic regions, followed by sublimation of the solvent, often followed by sintering to consolidate the structure (in ceramic suspensions).[6] A high degree of nano- and microstructural control over the as-cast aerogel is achieved by varying manufacturing

Received: May 28, 2021
Accepted: December 17, 2021
Published: February 8, 2022

https://doi.org/10.1021/acsnano.1c04538
ACS Nano 2022, 16, 1896–1908

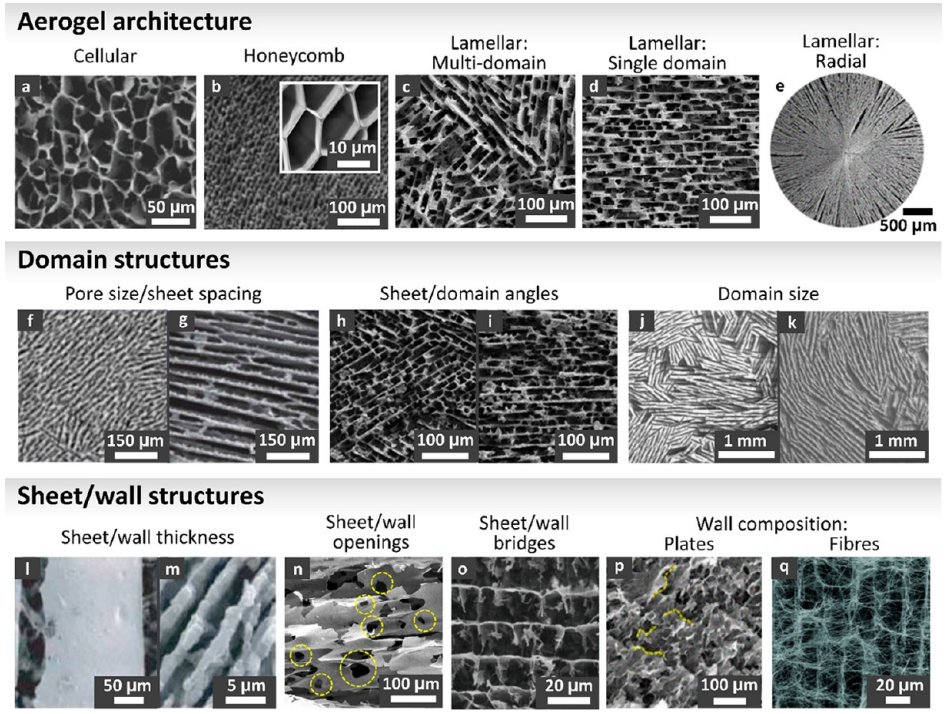

Figure 1. Structural features associated with aerogels. Aerogel architectures include (a) cellular,[10] (b) honeycomb,[11] (c) lamellar multidomain,[12] (d) lamellar single domain,[12] and (e) lamellar radial.[13] Typical domain structural parameters illustrating (f) small pore size/sheet spacing,[7] (g) larger pore size/sheet spacing.[7] (h) unaligned sheet/domain angles,[14] (i) greater alignment of sheet/domain angles,[14] (j) small domain size,[15] and (k) larger domain size.[15] Sheet/wall structural features include (l) large wall/sheet thickness,[16] (m) smaller wall/sheet thickness,[16] (n) wall/sheet openings,[2] (o) wall/sheet bridges,[10] (p) plate-like wall composition.[13] (q) fibrous wall composition.[17] (a,o) Reproduced with permission from ref 10. Copyright 2017 American Chemical Society. (b,b(inset)) Reproduced with permission from ref 11. Copyright 2008 ACS Publications. (c,d) Reproduced with permission from ref 12 Copyright 2019 under a Creative Commons CC BY 4.0 License from MDPI. (e,p) Reproduced with permission from ref 13. Copyright 2018, ACS Publications. (f,g) Reproduced with permission from ref 7. Copyright 2019 Elsevier. (h,i) Reproduced with permission from ref 14. Copyright 2012 Elsevier. (j,k) Reproduced with permission from ref 15. Copyright 2018 under a Creative Commons CC BY 4.0 License from MDPI. (l,m) Reproduced with permission from ref 16. Copyright 2006 American Association for the Advancement of Science. (n), Reproduced with permission from ref 2. Copyright 2019 American Chemical Society. (q) Reprinted with permission from ref 17. Copyright 2017 American Chemical Society.

parameters such as freezing rate, temperature gradient, colloid particle size, shape, and concentration, and use of different freezing agents or additives[7] enabling a wide range of architectures at the nano-, micro-, and mesoscales. Aerogels can display a wide range of microstructures including cellular, honeycomb, lamellar, and radial (Figure 1a–e) configurations. Aerogels often form domains which are clearly identifiable in lamellar structures; these domains can be tailored in terms of domain size, domain angles, and sheet spacing (Figure 1f–k). At the finest level they tend to comprise individual sheets, of varying sheet thickness, openings, and networks, and can be made up of plates or fibers for instance (Figure 1l–q).

For electrode applications, highly aligned sheets of high packing density are desirable to increase volumetric capacitance.[8] For composites, compressive straining allows a desired volume fraction of the aerogel phase to be attained prior to infiltration of a second material phase.[3] In sensors and oil cleanup applications, aerogels are designed for repeated use, whereby the sample must withstand many (>10 000 for sensors and >35 for oil cleanup, respectively) compression and relaxation cycles.[4,5] Across all applications, it is essential to determine what effects the nano- micro- and mesostructural features of a given aerogel have on its behavior during compression to predict and control domain collapse and to guide material design.[9]

Several methods have been used in the literature to study aerogel microstructures,[9,18] however, they have been used inconsistently across studies. Pycnometry and porometry can quantify porosity, the volume of the solid phase of the aerogel and specific surface area.[18] However, these methods give no indication of many features characteristic of aerogels which impact on functional properties, such as domain size or sheet inclination angle. Scanning electron microscopy (SEM) is commonplace for observation of aerogel sheet spacing and arrangement. While one can infer the 3D geometry from SEM imaging,[9] SEM is a surface imaging technique requiring cutting and stereology to assess internal structures. By contrast, X-ray computed microtomography (μCT) offers nondestructive 3D imaging, which also has the advantage that microstructural changes can be tracked over time. Synchrotron source μCT has previously been used to observe aerogel sheet and domain formation during freeze-casting in real-time,[19] to analyze aerogel structures resulting from varying manufacturing parameters,[20] and to follow *in situ* structural rearrangements of polymer foams during compression.[21] A particular challenge for the imaging of MXene aerogel is the aspect ratio of features of interest. The domains can span the full height of the sample (several mm) in the solidification direction, yet the thickness of lamellar sheets making up the domains can be as fine as tens of nanometers, produced from coalesced single-atom-thick particulates.[2] Synchrotron μCT lends itself to imaging high

https://doi.org/10.1021/acsnano.1c04538
ACS Nano 2022, 16, 1896–1908

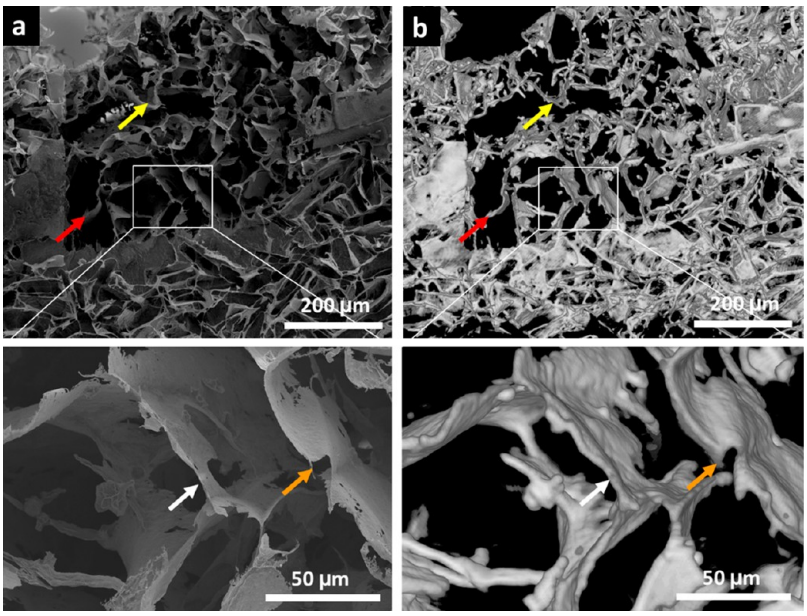

Figure 2. MXene aerogel sample with a section of the aerogel removed by plasma focused ion beam milling imaged at low (top) and high (bottom) magnification by (a) SEM and (b) laboratory source μCT in the form of a segmented 3D view (voxel size 1.25 μm). Arrows indicate the same features observed by both imaging techniques.

aspect-ratio features, as seen in aerogels, by taking advantage of phase contrast capability, as nanofiber studies have demonstrated.[22]

Visual inspection is often used to provide a qualitative assessment of aerogel domains,[23,24] however, automated quantitative image analysis offer a rapid, less-subjective alternative. Sheet spacing and sheet thickness can be determined using lines drawn perpendicular to sheet orientation, as commonly used for the analysis of 2D micrographs,[25] or using the ImageJ "local thickness" plugin,[20] which effectively computes the largest sphere that can fit within a pore space. A similar approach is to use a distance map to identify, separate, and quantitatively measure the pores between sheets, which has been successful in identifying and separating particles.[26] The ImageJ "directionality" plugin has also been used to identify domains based on orientation of the sheet-pore boundary,[27] but this method can be less accurate where sheet roughness is present.[28] Domain orientations can be determined via greyscale gradient using local Fourier transforms,[25] as proposed by Jeulin et al.[29] Here we determine sheet spacings using the distance map approach and identify domain orientations using the Fourier transform method.

Quantification and mapping of aerogel structure, in both the as-manufactured and in-service states, is necessary for the comparison and development of aerogels. We provide a framework for the quantitative analysis of aerogel domains using synchrotron phase contrast μCT (in our case using the ID15 beamline at the European Synchrotron Radiation Facility (ESRF)). Further, we characterize the collapse mechanisms that operate within this lamellar structure during uniaxial compression. This analysis has been applied to characterize the behavior of freeze-cast MXene (2D $Ti_3C_2T_x$) aerogel,[2] comprising 2D MXene, which is a class of material reported in 2011[30] and freeze-cast in 2019.[31] The collapse mechanisms and change in sheet spacing of MXene aerogels governs their electrochemical performance in supercapacitor applications,[2] and compression guided structural changes can influence mechanical properties for composite applications, therefore quantitative analysis of MXene aerogel compression offers scope to guide and control functional and mechanical properties. While the analysis methods discussed herein are widely applicable, this system demonstrates the capability of the method to quantify fine nanoscale features.

RESULTS AND DISCUSSION

Aerogel Visualization by μCT. A comparison of the same region of aerogel by SEM and μCT (see Figure 2) confirms that, despite the relatively large voxel size of the μCT ($(1.25\ \mu m)^3$) compared to the sheet thicknesses (1−18 stacked MXene flakes, corresponding to a thickness of 10−50 nm),[2] the great majority of the sheets are detected, however, it does mean that fine nanoscale features (see Figure 2d, orange arrow) appear to be thicker (1 voxel or more) than that revealed by SEM observations (Figure 2c, orange arrow). Similarly, the sheets appear to be much thicker when viewed by μCT when compared to SEM images (Figure 2c,d, white arrow). That they can be detected at all is in part due to the phase contrast which introduces fringes at the boundaries of features,[32] enhancing their visibility, but the coarse voxel size precludes recording their actual width. This makes the approach well suited to the imaging of the architectures and morphologies of the nanothickness aerogel sheets but not their volume fraction, wall thickness, or nanosized features, such as surface texture.

As-cast Aerogel Microstructure. A $4.2 \times 4.2 \times 10\ mm^3$ region in the center $10 \times 10 \times 10\ mm^3$ of the sample was imaged by synchrotron source μCT at a voxel size of 3.1 μm, permitting observation of many domains over the full height of the sample (Figure 3). The full data set has been made available online.[33−35] From this figure, it is clear that the aerogel exhibits a lamellar structure arranged in domains made up of equally spaced, parallel sheets of material. These domains are oriented such that their sheets are preferentially aligned with the freezing direction (Y) but with their plane normals "randomly" oriented in the XZ plane. Adjacent to the sample

https://doi.org/10.1021/acsnano.1c04538
ACS Nano 2022, 16, 1896−1908

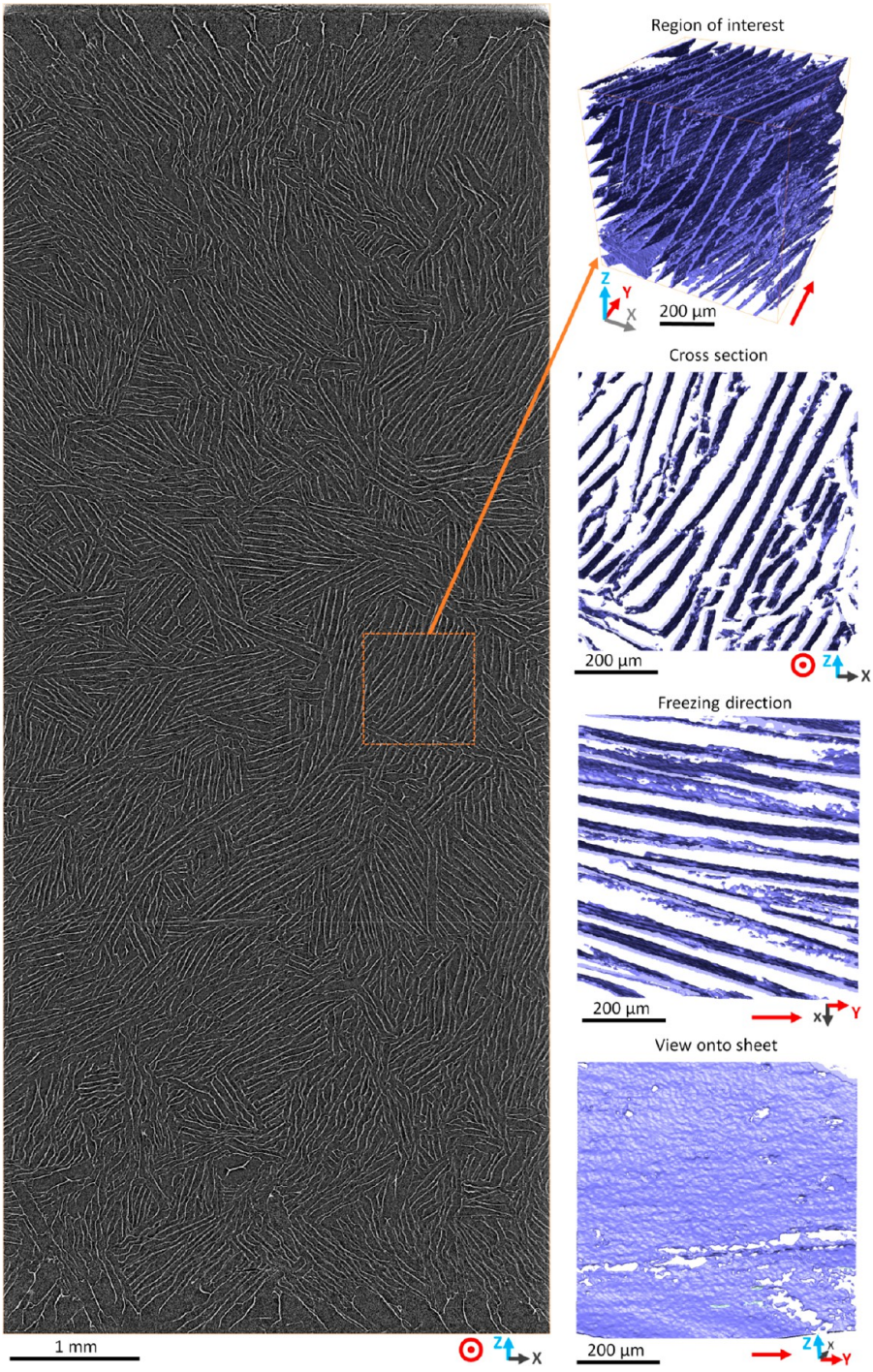

Figure 3. (left) Virtual CT cross-section (central slice) of the as-cast aerogel sample viewed on the *XZ* plane with the cast boundaries at the top and bottom, (right) a 3D rendering of a region of interest taken from within one domain, showing a perspective view and three orthogonal views from the region of interest (orthogonal views are 80 μm deep) (red vectors represent the freezing direction (*Y*)).

edge, at the top and bottom of the scanned volume, there is preferential alignment orthogonal to the sample edge. The structure of the domains and sheets are discussed in turn below.

Aerogel sheet orientation was determined using a custom Avizo module, which has been made available online.[36] To identify the domains and measure their orientation they have been classified according to the polar angle (φ) of their sheet normal relative to the loading direction (Z), binned in 10° increments, as illustrated in Figure 4 for a small region of interest. Alignment of the sheets with respect to the X direction of the sample is expressed in terms of the azimuthal angle (θ) projected by their plane normal. Looking at the scanned volume in Figure 5 segmented in this manner, it is clear that the domains are randomly orientated within the XZ plane except near the sample boundaries.

To assess the orientations of the sheets, the plane normals for all the planes in the scanned volume are plotted using a stereographic projection in Figure 6. This confirms that all the planes are oriented such that they are parallel to the freezing

https://doi.org/10.1021/acsnano.1c04538
ACS Nano 2022, 16, 1896−1908

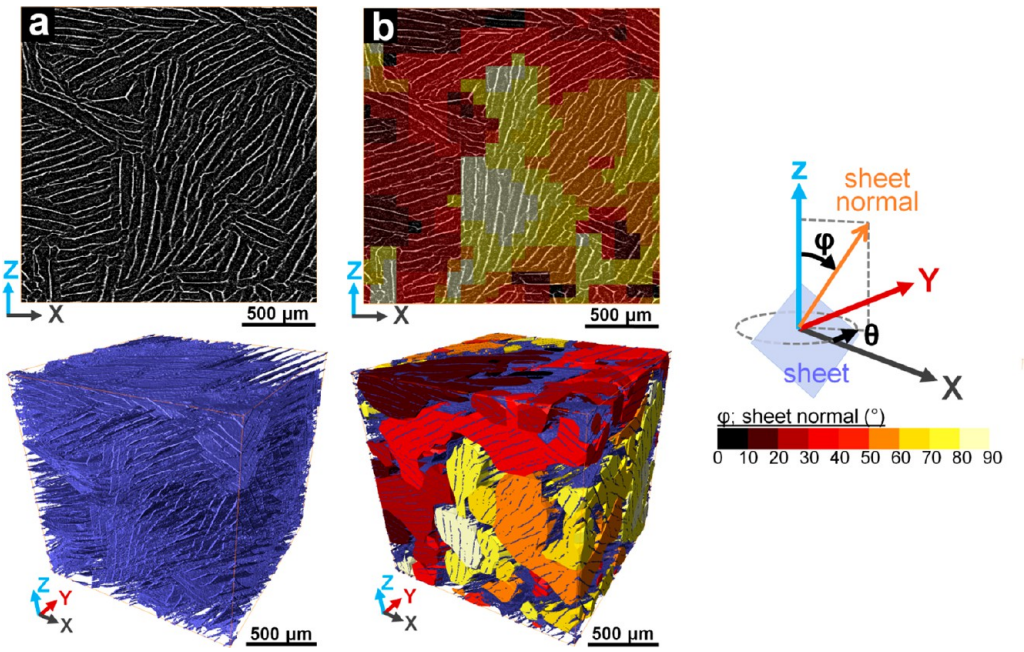

Figure 4. Region of interest taken from the center of the sample showing (a) A virtual CT section showing the aerogel sheets (white) (top) and a 3D segmented rendering of the aerogel sheets (bottom). (b) Virtual CT section showing the domain orientations segmented (in 10° bins from dark red to pale yellow) according to their sheet normal orientation (polar angle φ) (top) and the corresponding 3D segmented view of the domains alongside the aerogel sheets (bottom) (some of the voxels are rendered transparent to better visualize the 3D data in this image).

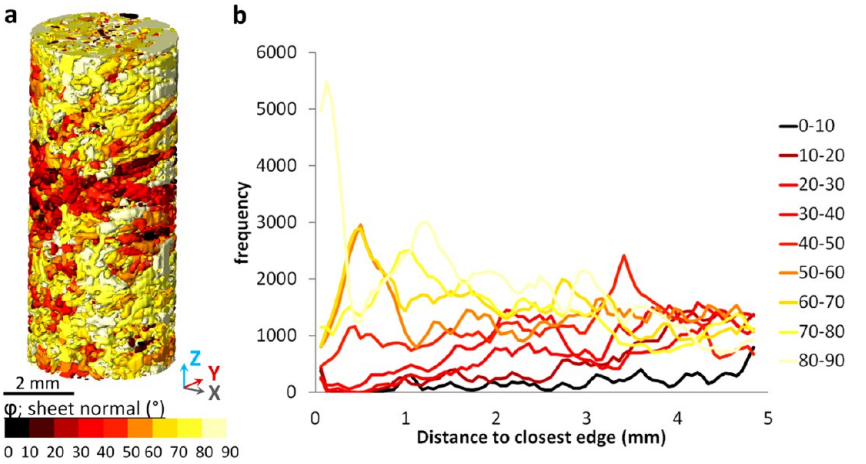

Figure 5. Scanned volume of the as-cast aerogel sample. (a) Volume rendering of segmented domains from μCT data (some voxels rendered transparent to ease visualization). (b) Analysis of the proximity of each voxel to the closest sample edge (top or bottom of the scanned volume) binned by sheet normal polar angle, φ (0° = horizontally aligned sheets, 90° = vertically aligned sheets).

direction (Y axis), with their plane normals all approximately randomly oriented in the XZ plane, although with a slight preference for angles close to the X-direction (Figure 6). The alignment of sheets with the freezing direction (Y) is not precise; the normal sheet angle interquartile range in θ was 21° (from −15° to 6°) with respect to X (Figure 6). The freezing rate is known to affect the alignment of the building blocks in the freezing direction.[37] Previous studies have found tilt about the freezing direction to be more prevalent at reduced aerogel freezing velocities, in particular, below 3−3.5 μm s^{-1}, with tilt of up to 4.5° being reported.[19] However, the freezing velocity in the present study, where unidirectional freezing was performed, was much higher at 15.43 μm s^{-1}, therefore the much higher tilt interquartile range of 21° was unexpected. This may be due to additional manufacturing parameters, such as the nature of the building blocks (cellulose microfibrils versus 2D sheets of MXenes) or induced directionality during freezing also affecting tilt, or could be due to differences in the methods of calculating sheet tilt between studies. Past literature has considered freeze-casting of other type of materials (cellulose, ceramics *etc.*), however, further investigation on the effect of different freezing velocities during freeze-casting of 2D materials would be of interest.

It is clear from Figure 5b and Figure 3 (left) that near the top and bottom of the scanned volume (adjacent to the mold surfaces) a large proportion of the domains are oriented in φ at 80−90°, i.e., normal to the mold wall. This distribution indicates that, unsurprisingly, sheet orientation is influenced by

https://doi.org/10.1021/acsnano.1c04538
ACS Nano 2022, 16, 1896−1908

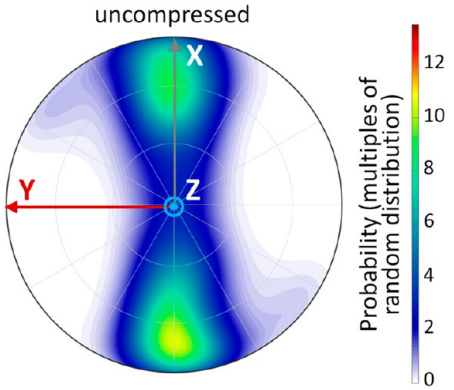

Figure 6. Stereographic projection showing the probability density function of the sheet normals throughout the imaged region of the as-cast sample (where a probability of 1 represents the expected density for a random distribution).

the mold walls during freezing, and further, that sheets closer to the edge may preferentially align normal to the wall. This effect has been seen previously in radial aerogels (Figure 1e).[13]

Within the domains, the mean sheet spacing was 33.0 (±11.1) μm throughout the whole scanned volume. There was no significant difference in sheet spacing in the as-cast sample (0% compression) when comparing domains of different angles, however, much larger sheet spacings are evident in Figure 3 in the domains adjacent to the mold walls (within ~400 μm of the top and bottom of the scanned volume), suggesting that sheet spacing is also influenced by the mold wall.

Microstructural Evolution during Compression. It is helpful to follow the structural changes that take place during compression at the three structural levels, namely at the level of the whole structure, the domains, and the sheets. At the level of the whole aerogel structure, the evolution of the aerogel during compression is shown in Figure 7, where bands of reorientation develop as neighboring domains with similar initial orientation all realign toward the horizontal (seen as dark bands developing in Figure 7 as compression increases). Observing the evolution of domain size and aspect ratio shows little change with compression (Figure 7). As the sample was compressed, the sheets within individual domains rotate (Figures 7 and 8), meaning that the normal of the aerogel sheets becomes more aligned with the loading direction (φ tends toward zero) with increasing compression. However, for those domains within 400 μm of the sample edge, where sheets are initially aligned perpendicular to the edge, the sheets do not reorient significantly (in φ) with increasing compression (Figure 8b), as discussed further below, although a reorientation in θ (the alignment with the freezing direction, *Y*, is apparent in this region.

The predominant intradomain behavior up to 50% compression is a reorientation of sheets toward the normal to the loading direction (*Z*) and simultaneous reduction in the sheet spacing (Figure 9a,b), with the exception of sheets initially aligned parallel with the loading direction ($\varphi \approx 80-90°$), which largely maintain their alignment and their sheet spacing (Figure 9c). Evidence of this is shown in Figure 9c, and quantitative evidence is provided from the analysis of the evolution of sheet spacing for domains of different angles (Figure 10). These site-specific behaviors give rise to the global behavior shown in Figure 8a of a reorientation toward the normal to the loading direction.

The resistance of domains oriented at $\varphi \approx 80-90°$ to rotation can explain the behavior of domains located within 400 μm of the sample edge. Here, little sheet rotation or compaction was seen in these domains up to 50% compression. Resistance to compaction at the sample edge is contrary to the behavior typical of cellular foams, which exhibit early failure in the zone adjacent to the platen due to a lack of lateral support at the edge.[38] Connectivity between sheets or walls may have less impact on aerogel collapse than it does in cellular foams, and instead, sheet orientation appears to be a more important factor in the compaction under compression.

Not all the similarly oriented domains behave the same. This is due to the different local environments, whereby the neighboring domains affect the behavior of a given domain, giving rise to localized interdomain behavior. Figure 9e shows a domain initially at $\varphi \sim 45°$, which exhibited a lower reduction in sheet spacing than expected during compression, however, the domain was constrained from rotation due to a neighboring domain of $\varphi \sim 90°$. Similarly, regions of shielding were also observed, whereby adjacent $\varphi \sim 90°$ domains prevented a reduction in the sheet spacing of neighboring domains (Figure 9c, white arrow).

While domains initially at $\varphi \sim 90°$ remained largely unchanged up to 50% compression, their sheets started to exhibit buckling at 60% compression such that by 80% compression their compressive strain is similar to surrounding grains, as observed during a complementary laboratory source μCT *in situ* compression study (Supporting Information, Figure S1). Sheets in smaller vertically aligned domains ($\varphi \sim 90°$) exhibit buckling before 50% compression (Figure 9b, red arrow), suggesting that domain size has an effect on the onset of deformation by buckling of domains aligned initially at $\varphi \sim 90°$.

The buckling and reorientation of domains initially at $\varphi \sim 90°$ has implications for applications where a single-domain aerogel is considered desirable, such as for energy storage materials, where sheet alignment impacts capacitance,[2] or in composite manufacture, where sheet alignment affects mechanical properties.[3,39] The development of an essentially uniform sheet spacing with an absence of large pores by 80% compression suggests that a single domain aerogel may not be necessary in the manufacture of compressed aerogel composites such as biomimetic nacre.[3,39] Similarly, aerogels for energy storage are typically manufactured with higher levels of compression (>80%) so may also not require a single domain aerogel.[2] Conversely, if compression of <50% is desired, a single domain lamellar aerogel (Figure 1d) may be better suited.

Simple modeling of the reorientation of the sheets under compression indicates that the reorientation and reduction in sheet spacing occur broadly in line with affine deformation for a material with a Poisson's ratio of zero (Figure 11). While this model does not include sheet buckling or interdomain effects (*e.g.*, shielding), a Poisson's ratio of zero is in agreement with the absence of lateral deformation during compression of the sample. While this predicted behavior (Figure 11a) largely agrees with the observed behavior (Figure 10), there are some notable differences. First, zero Poisson's ratio predicts no change in sheet spacing of domains oriented at $\varphi = 80-90°$, and second, a greater rate of change in sheet spacing is observed at 10% compression than that which is predicted, for

https://doi.org/10.1021/acsnano.1c04538
ACS Nano 2022, 16, 1896−1908

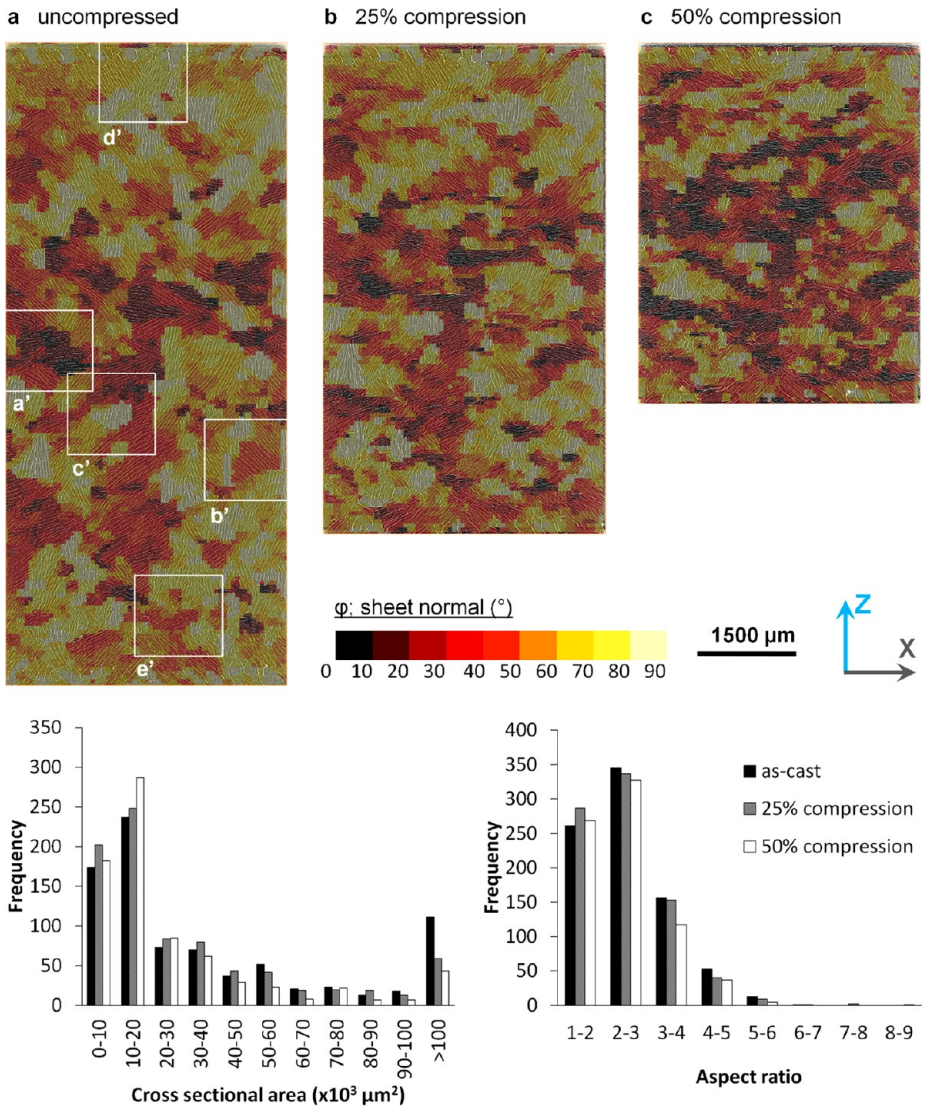

Figure 7. Aerogel structure and domain evolution during compression. (top) μCT data with overlaid colors indicating domain orientation identified by sheet normal polar angel, φ (0° = vertically aligned sheets, 90° = horizontally aligned sheets), (a) prior to compression, and evolution of the domains after (b) 25% compression and (c) 50% compression. All images represent the center slice of the scanned volume. The top and bottom of all three views correspond to the top and bottom of the sample adjacent to the compression platens. (In a, a′, b′, c′, and e′, highlight areas of interest where a domain is oriented at ∼0°, ∼ 45°, ∼ 90°, and ∼45° respectively. d′ highlights an area close to the sample edge. A magnified view of these highlighted areas are shown in Figure 9.) (bottom left) Domain cross sectional area in *XZ*. (bottom right) Aspect ratio of domain cross section in *XZ*, where 1 corresponds to a circular cross section.

all domain orientations. These differences may be due to interdomain effects and sheet buckling.

Zero Poisson's ratio has been observed previously in some cellular and lattice materials including cork[40] and semire-entrant honeycomb[41,42] and accordion honeycomb[43] structures which deform via undulating walls. Zero Poisson's ratio is desirable where lateral strain during tension or compression is undesirable, and such materials can also be formed into tube structures without saddle or doming which occurs with + ve and −ve Poisson's ratio, respectively, for potential use in tubular sandwich structures.[41] As with other zero Poisson's ratio materials, while the zero Poisson's ratio is an appropriate description of the material on a global level, this is not appropriate at finer scales of the hierarchical structure when considering the material itself which makes up the aerogel sheets.

It would be of interest to consider whether the findings of the present study are representative of the compressive deformation of aerogel microstructures in general, having different wall thicknesses, sheet spacing, bridges, and pore arrangements, along with nonlamellar aerogels (*e.g.*, honeycomb). Consequently, the extension of this work to aerogels produced with varying freeze-casting parameters is recommended in future work, and the quantification algorithms described here would be appropriate to quantifying a wide range of these. Additionally, obtaining the stress−strain curve during compression would enable linking between structural change and stress−strain response. Going forward, the development of methods to test the mechanical properties of walls is also recommended to enable identification of the relationship between wall properties and microstructural evolution during compression. Additionally, observing aerogel behavior during unloading would be of interest for applications

https://doi.org/10.1021/acsnano.1c04538
ACS Nano 2022, 16, 1896−1908

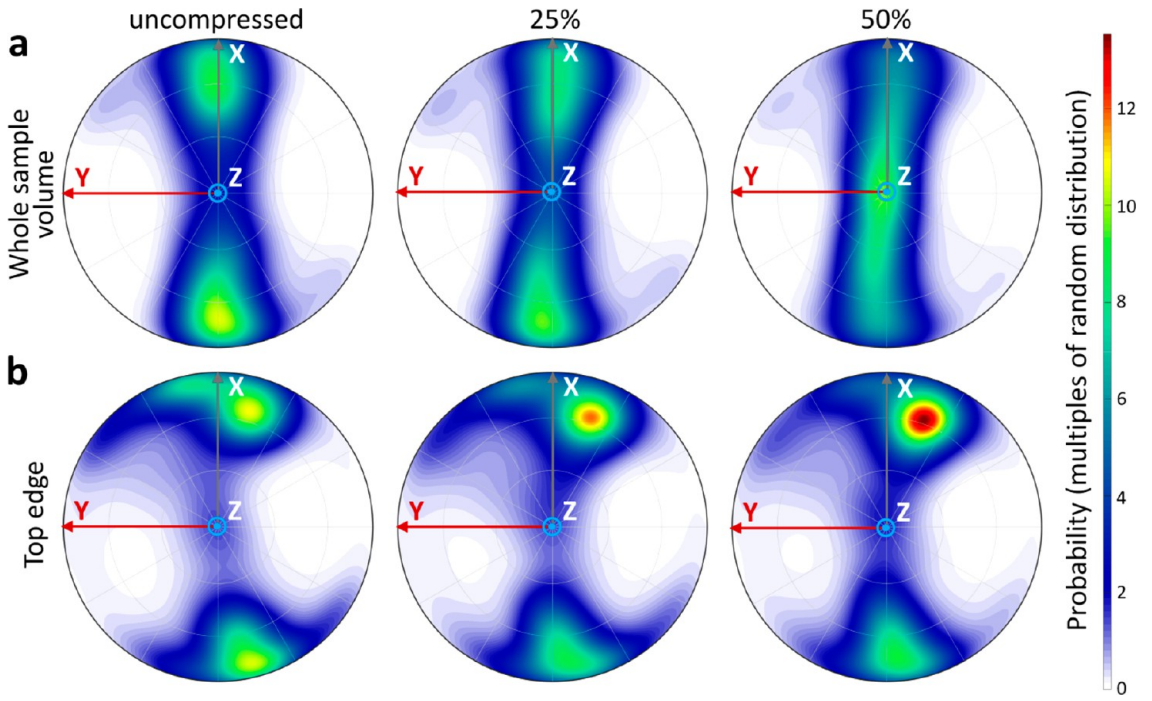

Figure 8. Stereographic projection showing the probability density function of the sheet normal directions (a) throughout the whole scanned volume and (b) the 400 μm adjacent to the top edge of the sample; before compression (left), after 25% compression (middle), and after 50% compression (right). Compression applied in the *Z* direction.

where repeated compression and relaxation cycles would be applied in-service. The analysis methods employed here can be also used to characterize the behavior or a wide variety of materials having a domain structure, either open structures such as the one considered here or infiltrated composite structures.

CONCLUSIONS

Compression allows a controlled modification of the lamellar aerogel structure, providing control over sheet orientation and spacing as a function of applied deformation, as revealed by μCT. Through the quantitative analysis of μCT images, we have developed methods to accurately characterize the freeze-cast aerogel across multiple scales of this hierarchical structure and to monitor their evolution as a function of processing. This allows for more precise engineering of the microstructure through the application of well-defined straining.

Compressive straining (up to 50% strain) results in progressive realignment of sheets normal to the loading direction along with reduction in sheet spacing, with the exception of domains initially aligned with the loading direction which maintain orientation and sheet spacing until buckling, which results in large pore opening.

The compression behavior observed experimentally is broadly in agreement with a Poisson's ratio of zero. Indeed, lamellar aerogels may find applications where lateral deformation is unwanted, such as where the material will be formed into tubular structure, or in developing composites which exhibit no lateral strain.

EXPERIMENTAL METHODS

Aerogel Sample Manufacture. The MXene aerogels were prepared as described by Bayram *et al.*[2] Briefly, 2D $Ti_3C_2T_x$ (titanium carbide, particle size ~2 μm) were produced via selective etching of Al layer from MAX phase-Ti_3AlC_2 (titanium aluminum carbide) (Drexel University, USA). The resulting reaction mixture was washed several times to reach a pH above 6. The 2D $Ti_3C_2T_x$ in degassed water were exfoliated with sonication for 1 h at room temperature, and then the concentration of the 2D $Ti_3C_2T_x$ in water was adjusted to 15 mg/mL. Next, 0.75 mL of the particle suspension was poured into a PTFE mold, with a 1 cm × 1 cm square base, which was attached to a copper coldfinger. No binders or additives were added to the colloidal solution. The solution was then frozen down to −70 °C starting from RT, with a freezing rate of 5 °C/min. Once frozen, samples were transferred to a freeze-drier (FreezeZone, Labcanco, USA) and freeze-dried for 48 h, leaving the intact 10 mm cubic aerogel structure. Visual inspection confirmed that freeze-drying did not result in significant sample shrinkage.

Comparing Focused Ion Beam-SEM with Laboratory μCT Imaging. An aerogel sample was mounted to a 45° pretilted sample holder using silver paint with the bottom surface of the aerogel (the surface adjacent to the coldfinger during freeze-casting) facing upward, then allowed to dry at room temperature overnight. A fresh surface was cut from the edge of the sample using an FEI Xe^+ plasma focused ion beam, operated under 30 keV and 0.18 μA (FEI HELIOS Plasma FIB and SEM; Thermo Fisher Scientific, MA, US). This exposed the internal microstructures of the aerogel, which was then imaged using SEM at 5 keV and 85 pA.

The sample, still adhered to the pretilted SEM sample holder, was next loaded into a Versa XRM-520 (Zeiss, Oberkochen, Germany) controlled by XRM scout-and-scan control system (v.1.1.5707.17179; Zeiss, Oberkochen, Germany), and the notched region of the sample was μCT imaged. Voltage and power were set to 70 kV and 6 W, respectively. The source to sample and sample to detector distances were 43 and 73 mm, respectively, along with 4× magnification, resulting in an isotropic voxel size of 1.25 μm and scanned volume of 2.5 × 2.5 × 2.5 mm^3. The 3001 projections were taken through 360° of rotation using 75 s exposure time. This imaging setup provided some phase contrast, which enhanced visibility of aerogel sheets.

Data was reconstructed using Zeiss Scout-and-Scan reconstructor (Zeiss, Oberkochen, Germany), followed by visualization using Avizo (version 2019.3; Visualization Sciences Group, Oregon, USA). No filter was used during imaging analysis and segmentation was

https://doi.org/10.1021/acsnano.1c04538
ACS Nano 2022, 16, 1896−1908

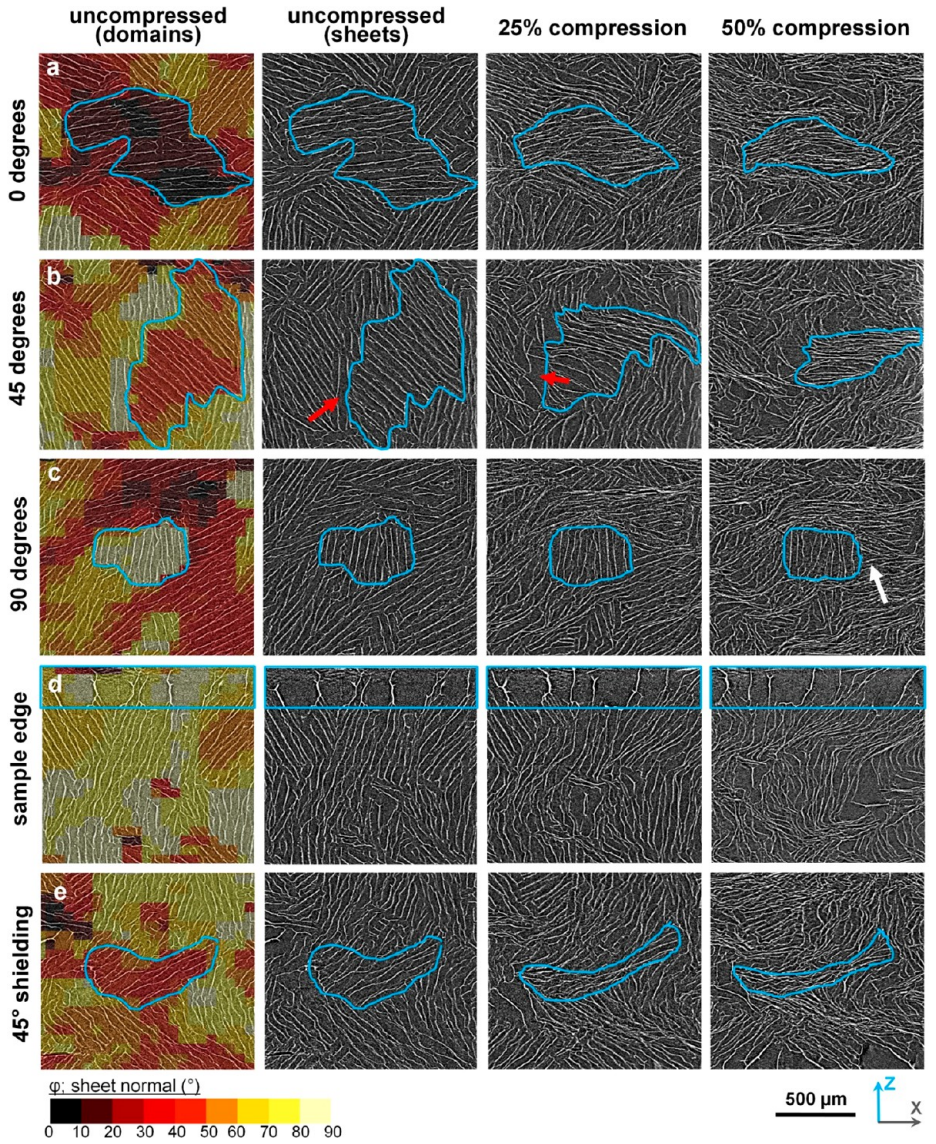

Figure 9. Subvolumes of the CT data in the central slice, showing (a) sheet spacing reduction, initially 0° φ orientation; (b) sheet spacing reduction and rotation, initially 45° φ orientation; (c) buckling, initially 90° φ orientation, (d) the sample edge (e) shielding, initially 45° φ orientation. Figure shows (far left) uncompressed sheets with overlaid domains (identified by sheet normal polar angle, φ), (mid left) uncompressed sheets, (mid right) sheets following 25% compression, and (far right) sheets after 50% compression. (a–e correspond to Figure 7a,; a′, b′, c′, d′, and e′. Blue line = domain of interest, red arrows = sheet buckling and pore opening (buckling also seen within the highlighted (d) domain), white arrow = shielding region.)

performed manually based on greyscale thresholding of interconnected voxels.

Synchrotron μCT Imaging and *in Situ* Compression. A custom-made rig was manufactured to compress the aerogel sample to a given height and then maintain the position during μCT imaging. The rig consisted of a polystyrene chamber (1 mm wall thickness) in which the sample was compressed between two flat acrylic platens. Compression was driven by the turning of four nuts along threaded rods, which, in turn, depressed the top platen; one full rotation of the nuts depressed the sample by 0.5 mm. Samples were loaded as-cast into the compression chamber in the orientation shown in Figure 12. The sample was imaged without compression, followed by subsequent scans after compression increments of 5% strain to a maximum of 50% strain. Compression was applied aligned with the Z axis (perpendicular to the freezing direction) (Figure 12).

Synchrotron μCT imaging was performed at the European Synchrotron Radiation Facility on the ID15A beamline. Imaging was performed at 40 keV energy and 100 ms exposure time, taking 1500 projections around 180° of sample rotation. Sample to detector distance was 100 mm to allow some in-line phase contrast in order to enhance visibility of the aerogel sheets. This provided a voxel size of 3.2 μm and a 4.4 mm field of view to image the central portion of the sample. Reconstruction was performed using a filtered back projection algorithm provided by ESRF. Up to three scans were taken at each compression step in order to image the full height (in Z) of the sample, which were later stitched together manually using Avizo (version 2019.3; FEI Visualization Sciences Group). The μCT data sets have been made available.[33−35]

Microstructural Analysis; Sheet Orientation and Domains. Sheet orientation and domain analyses are summarized in Figure 13. Sheet orientation was determined using a custom-written Avizo module,[36] which divided the 3D data set into user defined subvolumes and computed the fast Fourier transform of each subvolume. By determining the eigenvector associated with the minimum eigenvalue of the inertia matrix of the Fourier transformed block, the custom Avizo module outputs the vector normal to the aerogel sheets within each subvolume, defined by angles φ and θ (Figure 4). The optimal subvolume size was determined to be 20 voxels for the present data

https://doi.org/10.1021/acsnano.1c04538
ACS Nano 2022, 16, 1896−1908

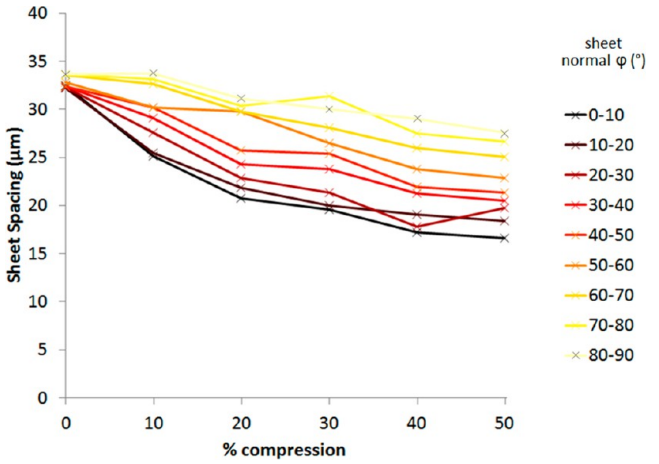

Figure 10. Sheet spacing within the domains as a function of the degree of compression, according to sheet normal polar angle, φ.

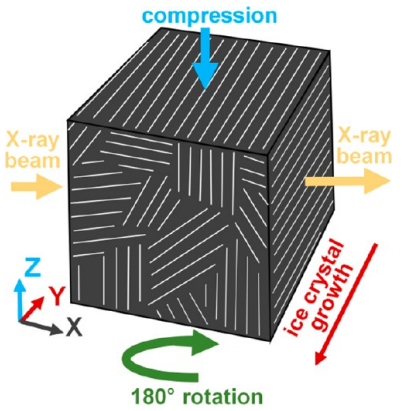

Figure 12. Sample orientation during imaging and compression.

and used throughout. Angle φ defines the orientation of sheets with respect to the axis of applied compression (Z axis), of interest to determine how sheets realign with increasing compressive strain. To discern between and visualize aerogel domains, the data set defining φ

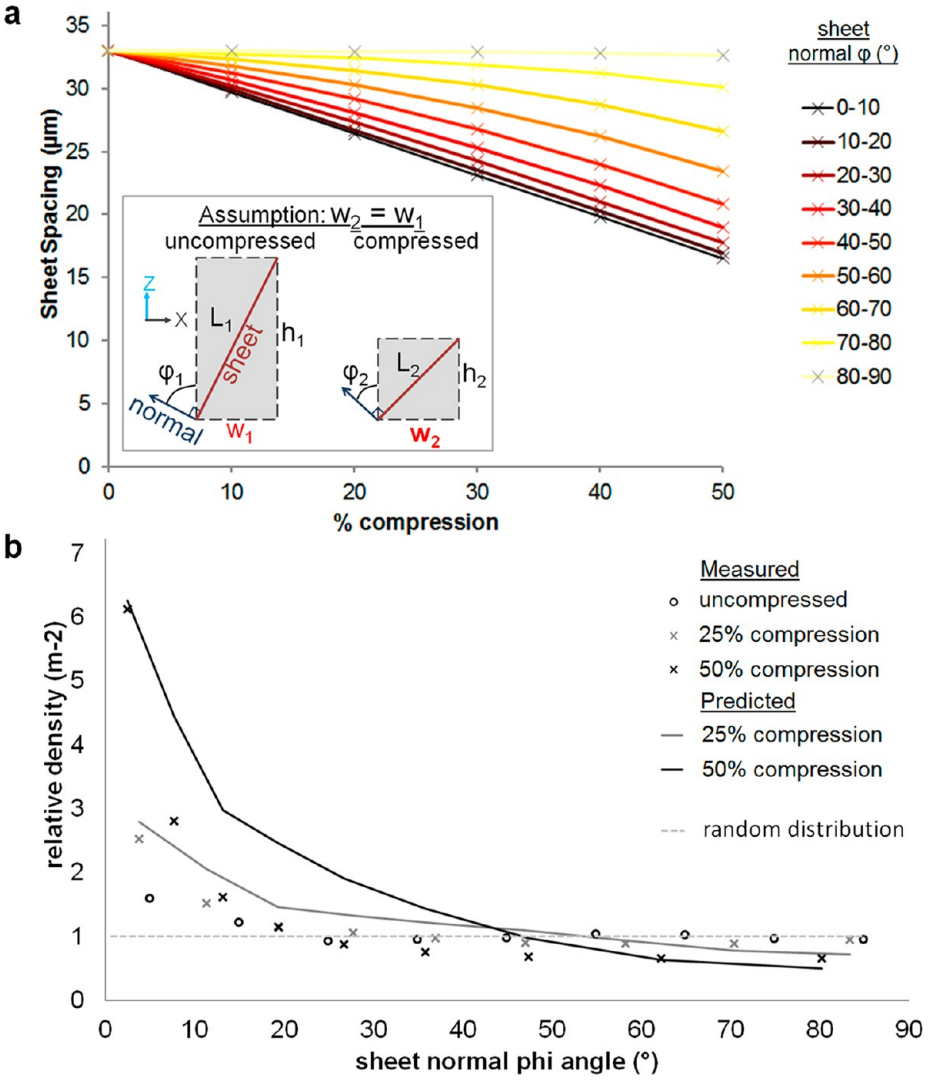

Figure 11. Evolution of aerogel during compression, predicted by assuming zero Poisson's ratio. (a) Predicted change in sheet spacing for domains of different initial sheet normal polar angle (φ). (Inset) Schematic of the assumed behavior (zero Poisson's ratio). (b) Distribution of sheet normal polar angle (φ) expressed as relative density whereby values of 1 for all angles would represent a random distribution, comparing experimental measurements with predicted values.

https://doi.org/10.1021/acsnano.1c04538
ACS Nano 2022, 16, 1896−1908

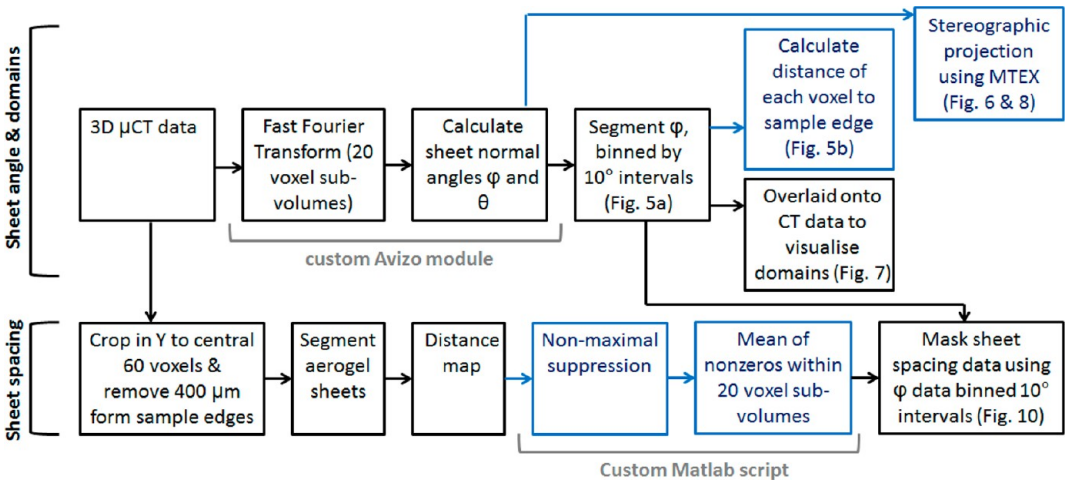

Figure 13. Flowchart summarizing analysis of sheet angle, domains, and sheet spacing (black = steps performed within Avizo; blue = steps performed within Matlab).

(which ranged between 0° and 90°) was binned into 10° intervals and segmented. This defined all neighboring voxels as belonging to the same domain if φ was within the same 10° interval. The segmentation was then smoothed in 3D using a smoothing factor of 2. The segmented domains were overlaid onto the CT data for visualization. Domain cross sectional area and ferret shape (aspect ratio) were calculated in *XZ* on the center slice using the label analysis module in Avizo.

To determine the positional distribution of domains, the distance from the closest sample edge (being the upper or lower boundaries of the scanned volume; Figure 3) was calculated for each voxel, for each 10° interval, using Matlab[44] (2017a, Mathworks, MA, US). Sheet normal azimuth (θ) and polar (φ) angles were imported into Matlab, and the stereographic projection probability density function was plotted using the MTEX Toolbox (MTEX v5.4.0; open source software available at https://mtex-toolbox.github.io/download).

Microstructural Analysis: Sheet Spacing. The sheet spacing analysis method is summarized in Figure 13. 3D sheet spacing analysis was performed on a cropped data set to allow practical computational time; data was cropped in *Y* such that the center 60 voxels remained. Data was also cropped in *Z* to remove 400 μm adjacent to the sample edges (top and bottom of scanned volume), where very large sheet spacing, uncharacteristic of sample midsubstance, was apparent (Figure 3). Using Avizo, aerogel sheets were segmented, and then the distance map was computed using the Euclidian method, which assigns each voxel with the distance from the nearest segmented voxel (in this case, the distance from aerogel sheets). The distance map was exported as a 16 bit unsigned 2D tif stack. Sheet spacing was then computed using Matlab by performing nonmaximal suppression (using a 3 × 3 × 3 voxel search window) to remove all but local maxima distance map values, which was then multiplied by 2 (necessary because the distance map local maxima values are half the local distance between sheets). The mean of nonzero values within a 20 voxel search window was then calculated to produce the sheet spacing matrix (excluding values less than 2, which represents sheet roughness)[45] which was then imported back into Avizo. The segmented domains (produced during the sheet orientation and domain analysis) were used to mask the sheet spacing matrix, which effectively separated sheet spacing data by sheet normal angle φ (binned into 10° angle intervals), allowing mean sheet spacing to be plotted against sheet normal angle φ for each compression step.

Predicting the Compressive Response. Predictions were made of how the distribution of domain φ angle would change with compression, under three different assumed behaviors: zero Poisson's ratio, constant volume, and constant sheet length. Taking the domain angles for the initial, uncompressed sample, the compressed sheet angles (at 25% and 50% compression) were calculated for the three assumed behaviors. Data was presented as sheet spacing for different sheet normal polar angles (φ) at different compression steps and as relative density, representing multiples of random distribution where fully randomly distributed sheet angles would be represented by a value of 1 for all angles. Only the zero Poisson's ratio prediction has been presented, which represented the closest agreement with experimental data.

ASSOCIATED CONTENT

Supporting Information

The Supporting Information is available free of charge at https://pubs.acs.org/doi/10.1021/acsnano.1c04538.

Laboratory source μCT study of aerogel compression, imaged prior to compression, then following 20%, 40%, 60%, and 80% strain (PDF)

AUTHOR INFORMATION

Corresponding Author

Shelley D. Rawson − *Henry Royce Institute, Department of Materials, The University of Manchester, Manchester M13 9PL, U.K.;* orcid.org/0000-0002-9407-4072; Email: shelley.rawson@manchester.ac.uk

Authors

Vildan Bayram − *Department of Materials, University of Manchester, Manchester M13 9PL, U.K.;* orcid.org/0000-0001-9781-4980

Samuel A. McDonald − *MAX IV Laboratory, Lund 224 84, Sweden*

Pei Yang − *Department of Materials, University of Manchester, Manchester M13 9PL, U.K.;* orcid.org/0000-0002-4639-2076

Loic Courtois − *3Dmagination, Harwell, Oxford OX11 0QX, U.K.*

Yi Guo − *Department of Materials, Imperial College London, London SW7 2BU, U.K.;* Present Address: Shenyang National Laboratory for Materials Science, Institute of Metal Research, Chinese Academy of Science, 72 Wenhua Road, Shenyang 110016, PR China

Jiaqi Xu − *Henry Royce Institute, Department of Materials, The University of Manchester, Manchester M13 9PL, U.K.*

Timothy L. Burnett − *Henry Royce Institute, Department of Materials, The University of Manchester, Manchester M13 9PL, U.K.*

https://doi.org/10.1021/acsnano.1c04538
ACS Nano 2022, 16, 1896−1908

Suelen Barg − *Department of Materials, University of Manchester, Manchester M13 9PL, U.K.; Institute of Materials Resource Management, Augsburg University, Augsburg 86159, Germany;* orcid.org/0000-0002-0723-7081

Philip J. Withers − *Henry Royce Institute, Department of Materials, The University of Manchester, Manchester M13 9PL, U.K.*

Complete contact information is available at: https://pubs.acs.org/10.1021/acsnano.1c04538

Notes

The authors declare no competing financial interest.

ACKNOWLEDGMENTS

With thanks to the European Research Council for the funding given for Micro-CT studies, which was provided under the European Commission's Horizon 2020 (FP8/2014-2020) ERC advanced grant agreement number 695638 (CORREL-CT). We acknowledge the European Synchrotron Radiation Facility for provision of synchrotron radiation facilities, and we thank Thomas Buslaps for assistance in using beamline ID15A. Thanks also to 3Dmagination for producing the custom Avizo module to determine aerogel sheet orientation. V.B. thanks the Newton-Katip Celebi Fund provided by The Scientific and Technological Research Council of Turkey (TUBITAK) and British Council. We also like to thank Dr. Christopher Daniel and Dr. Ali Gholinia for support in the use of MTEX to visualise the probability density function. We thank the Henry Moseley X-ray Imaging Facility (HMXIF), which is supported through EPSRC grant nos. EP/M010619, EP/K004530, EP/F007906, EP/F001452, EP/I02249X, and EP/F028431. The HMXIF is part of the National Research Facility for Lab X-ray CT, which is supported through EPSRC grant EP/T02593X/1. This work was also supported by the Henry Royce Institute for Advanced Materials, funded through EPSRC grants EP/R00661X/1, EP/S019367/1, EP/P025021/1, and EP/P025498/1.

REFERENCES

(1) Woignier, T.; Duffours, L. Densification and Strengthening of Aerogels by Sintering Heat Treatments or Plastic Compression. *Gels* **2018**, *4* (12), 12.

(2) Bayram, V.; Ghidiu, M.; Byun, J. J.; Rawson, S. D.; Yang, P.; Mcdonald, S. A.; Lindley, M.; Fairclough, S.; Haigh, S. J.; Withers, P. J.; et al. MXene Tunable Lamellae Architectures for Supercapacitor Electrodes. *ACS Applied Energy Materials* **2020**, *3*, 411−422.

(3) Bai, H.; Walsh, F.; Gludovatz, B.; Delattre, B.; Huang, C.; Chen, Y.; Tomsia, A. P.; Ritchie, R. O. Bioinspired Hydroxyapatite/Poly(methyl Methacrylate) Composite with a Nacre-Mimetic Architecture by a Bidirectional Freezing Method. *Adv. Mater.* **2016**, *28* (1), 50−6.

(4) Ma, Y.; Yue, Y.; Zhang, H.; Cheng, F.; Zhao, W.; Rao, J.; Luo, S.; Wang, J.; Jiang, X.; Liu, Z.; Liu, N.; Gao, Y. 3D Synergistical MXene/Reduced Graphene Oxide Aerogel for a Piezoresistive Sensor. *ACS Nano* **2018**, *12* (4), 3209−3216.

(5) Zhang, X.; Wang, H.; Cai, Z.; Yan, N.; Liu, M.; Yu, Y. Highly Compressible and Hydrophobic Anisotropic Aerogels for Selective Oil/Organic Solvent Absorption. *ACS Sustaibale Chemistry and Engnieering* **2019**, *7* (1), 332−340.

(6) Waschkies, T.; Oberacker, R.; Hoffmann, M. J. Control of Lamellae Spacing during Freeze Casting of Ceramics Using Double-Side Cooling as a Novel Processing Route. *Juornal of the American Ceramic Society* **2009**, *92* (S1), S79−S84.

(7) Nelson, I.; Naleway, S. E. Intrinsic and Extrinsic Control of Freeze Casting. *Journal of Materials Research and Technology* **2019**, *8* (2), 2372−2385.

(8) Tao, Y.; Xie, X.; Lv, W.; Tang, D. M.; Kong, D.; Huang, Z.; Nishihara, H.; Ishii, T.; Li, B.; Golberg, D.; Kang, F.; Kyotani, T.; Yang, Q. H. Towards Ultrahigh Volumetric Capacitance: Graphene Derived Highly Dense but Porous Carbons for Supercapacitors. *Sci. Rep* **2013**, *3*, 2975.

(9) Ma, H.; Zheng, X.; Luo, X.; Yi, Y.; Yang, F. Simulation and Analysis of Mechanical Properties of Silica Aerogels: From Rationalization to Prediction. *Materials (Basel)* **2018**, *11*, 214.

(10) Yang, M.; Zhao, N.; Cui, Y.; Gao, W.; Zhao, Q.; Gao, C.; Bai, H.; Xie, T. Biomimetic Architectured Graphene Aerogel with Exceptional Strength and Resilience. *ACS Nano* **2017**, *11* (7), 6817−6824.

(11) Gutiérrez, M. C.; Ferrer, M. L.; del Monte, F. Ice-Templated Materials: Sophisticated Structures Exhibiting Enhanced Functionalities Obtained after Unidirectional Freezing and Ice-Segregation-Induced Self-Assembly. *Chem. Mater.* **2008**, *20* (3), 634−648.

(12) Niksiar, P.; Su, F. Y.; Frank, M. B.; Ogden, T. A.; Naleway, S. E.; Meyers, M. A.; McKittrick, J.; Porter, M. M. External Field Assisted Freeze Casting. *Ceramics* **2019**, *2* (1), 208−234.

(13) Wang, C.; Chen, X.; Wang, B.; Huang, M.; Wang, B.; Jiang, Y.; Ruoff, R. S. Freeze-Casting Produces a Graphene Oxide Aerogel with a Radial and Centrosymmetric Structure. *ACS Nano* **2018**, *12* (6), 5816−5825.

(14) Porter, M. M.; Yeh, M.; Strawson, J.; Goehring, T.; Lujan, S.; Siripasopsotorn, P.; Meyers, M. A.; McKittrick, J. Magnetic Freeze Casting Inspired by Nature. *Materials Science and Engineering: A* **2012**, *556*, 741−750.

(15) Hautcoeur, D.; Gonon, M.; Baudin, C.; Lardot, V.; Leriche, A.; Cambier, F. Alumina Porous Ceramics Obtained by Freeze Casting: Structure and Mechanical Behaviour under Compression. *Ceramics* **2018**, *1* (1), 83−97.

(16) Deville, S.; Saiz, E.; Nalla, R. K.; Tomsia, A. P. Freezing as a Path to Build Complex Composites. *Science* **2006**, *311* (5760), 515−518.

(17) Qian, F.; Lan, P. C.; Freyman, M. C.; Chen, W.; Kou, T.; Olson, T. Y.; Zhu, C.; Worsley, M. A.; Duoss, E. B.; Spadaccini, C. M.; et al. Ultralight Conductive Silver Nanowire Aerogels. *Nano Lett.* **2017**, *17* (12), 7171−7176.

(18) Fricke, J.; Emmerling, A. Aerogels - Preparation, Properties, Applications. *Struct. Bonding (Berlin)* **1992**, *77*, 37−87.

(19) Deville, S.; Adrien, J.; Maire, E.; Scheel, M.; Di Michiel, M. Time-Lapse, Three-Dimensional *in Situ* Imaging of Ice Crystal Growth in a Colloidal Silica Suspension. *Acta Mater.* **2013**, *61* (6), 2077−2068.

(20) Ghafar, A.; Parikka, K.; Haberthur, D.; Tenkanen, M.; Mikkonen, K. S.; Suuronen, J. P. Synchrotron Microtomography Reveals the Fine Three-Dimensional Porosity of Composite Polysaccharide Aerogels. *Materials (Basel)* **2017**, *10*, 871.

(21) Patterson, B. M.; Cordes, N. L.; Henderson, K.; Williams, J. J.; Stannard, T.; Singh, S. S.; Ovejero, A. R.; Xiao, X.; Robinson, M.; Chawla, N. *In Situ* X-Ray Synchrotron Tomographic Imaging during the Compression of Hyper-Elastic Polymeric Materials. *J. Mater. Sci.* **2016**, *51* (1), 171−187.

(22) Maksimcuka, J.; Obata, A.; Sampson, W. W.; Blanc, R.; Gao, C.; Withers, P. J.; Tsigkou, O.; Kasuga, T.; Lee, P. D.; Poologasundarampillai, G. X-Ray Tomographic Imaging of Tensile Deformation Modes of Electrospun Biodegradable Polyester Fibers. *Fron. Mater.* **2017**, *4*, 43.

(23) Deville, S.; Maire, E.; Lasalle, A.; Bogner, A.; Gauthier, C.; Leloup, J.; Guizard, C. *In Situ* X-Ray Radiography and Tomography Observations of the Solidification of Aqueous Alumina Particle Suspension-Part 1: Initial Instants. *J. Am. Ceram. Soc.* **2009**, *92* (11), 2489−2496.

(24) Lichtner, A.; Roussel, D.; Jauffrès, D.; Martin, C. L.; Bordia, R. K. Effect of Macropore Anisotropy on the Mechanical Response of

Hierarchically Porous Ceramics. *J. Am. Ceram. Soc.* **2016**, *99* (3), 979−987.
(25) Bai, H.; Chen, Y.; Delattre, B.; Tomsia, A. P.; Ritchie, R. O. Bioinspired Large-Scale Aligned Porous Materials Assembled with Dual Temperature Gradients. *Sci. Adv.* **2015**, *1*, No. e1500849.
(26) Alam, M. F.; Haque, A. A New Cluster Analysis-Marker-Controlled Watershed Method for Separating Particles of Granular Soils. *Materials* **2017**, *10* (10), 1195.
(27) Bouville, F.; Portuguez, E.; Chang, Y.; Messing, G. L.; Stevenson, A. J.; Maire, E.; Courtois, L.; Deville, S. Templated Grain Growth in Macroporous Materials. *J. Am. Ceram. Soc.* **2014**, *97* (6), 1736−1742.
(28) Deville, S., Freezing Colloids: Observations, Principles, Control, and Use: Applications in Materials Science, Life Science, *Earth Science, Food Science, and Engineering*; Springer International: Cham, 2017.
(29) Jeulin, D.; Moreaud, M. Segmentation of 2D and 3D Textures from Estimates of the Local Orientation. *Image Analysis & Stereology* **2008**, *27* (3), 183−192.
(30) Naguib, M.; Kurtoglu, M.; Presser, V.; Lu, J.; Niu, J.; Heon, M.; Hultman, L.; Gogotsi, Y.; Barsoum, M. W. Two-Dimensional Nanocrystals Produced by Exfoliation of Ti3AlC2. *Advanced materials* **2011**, *23* (37), 4248−4253.
(31) Tontini, G.; Greaves, M.; Ghosh, S.; Bayram, V.; Barg, S. MXene-Based 3D Porous Macrostructures for Electrochemical Energy Storage. *Journal of Physics: Materials* **2020**, *3* (2), 022001.
(32) Yu, B.; Bradley, R.; Soutis, C.; Withers, P. A Comparison of Different Approaches for Imaging Cracks in Composites by X-Ray Microtomography. *Philosophical Transactions of the Royal Society A: Mathematical, Physical and Engineering Sciences* **2016**, *374* (2071), 20160037.
(33) Rawson, S. D.; Bayram, V.; McDonald, S. A.; Yang, P.; Courtois, L.; Guo, Y.; Xu, J.; Burnett, T. L.; Barg, S.; Withers, P. J. CT Data: Freeze Cast Aerogel As-Cast and Following Compressive Strain. *Zenodo*; CERN, 2021; upload 2 of 3, DOI: 10.5281/zenodo.4761663 (accessed 2021-05-27).
(34) Rawson, S. D.; Bayram, V.; McDonald, S. A.; Yang, P.; Courtois, L.; Guo, Y.; Xu, J.; Burnett, T. L.; Barg, S.; Withers, P. J. CT Data: Freeze Cast Aerogel As-Cast and Following Compressive Strain, *Zenodo*; CERN, 2021; upload 2 of 3, DOI: 10.5281/zenodo.4764282 (accessed 2021-05-27).
(35) Rawson, S. D.; Bayram, V.; McDonald, S. A.; Yang, P.; Courtois, L.; Guo, Y.; Xu, J.; Burnett, T. L.; Barg, S.; Withers, P. J. CT Data: Freeze Cast Aerogel As-Cast and Following Compressive Strain. *Zenodo*; CERN, 2021; upload 3 of 3, DOI: 10.5281/zenodo.4766087 (accessed 2021-05-27).
(36) Rawson, S. D.; Bayram, V.; McDonald, S. A.; Yang, P.; Courtois, L.; Guo, Y.; Xu, J.; Burnett, T. L.; Barg, S.; Withers, P. J. CT Analysis: Orientation of Lamellar Sheets Avizo Module. *Zenodo*; CERN, 2021; upload 1, DOI: 10.5281/zenodo.4748721 (2021-05-27).
(37) Zhang, X.; Yu, Y.; Jiang, Z.; Wang, H. The Effect of Freezing Speed and Hydrogel Concentration on the Microstructure and Compressive Performance of Bamboo-Based Cellulose Aerogel. *Journal of Wood Science* **2015**, *61* (6), 595−601.
(38) Brezny, R.; Green, D. Characterization of Edge Effects in Cellular Materials. *J. Mater. Sci.* **1990**, *25* (11), 4571−4578.
(39) Tan, G.; Zhang, J.; Zheng, L.; Jiao, D.; Liu, Z.; Zhang, Z.; Ritchie, R. O. Nature-Inspired Nacre-Like Composites Combining Human Tooth-Matching Elasticity and Hardness with Exceptional Damage Tolerance. *Adv. Mater.* **2019**, *31* (52), 1904603.
(40) Pereira, H. The Rationale Behind Cork Properties: A Review of Structure and Chemistry. *BioResources* **2015**, *10*, 6207−6229.
(41) Attard, D.; Grima, J. N. Modelling of Hexagonal Honeycombs Exhibiting Zero Poisson's Ratio. *physica status solidi (b)* **2011**, *248* (1), 52−59.
(42) Soman, P.; Fozdar, D. Y.; Lee, J. W.; Phadke, A.; Varghese, S.; Chen, S. A Three-Dimensional Polymer Scaffolding Material Exhibiting a Zero Poisson's Ratio. *Soft Matter* **2012**, *8* (18), 4946−4951.
(43) Olympio, K. R.; Gandhi, F. Zero Poisson's Ratio Cellular Honeycombs for Flex Skins Undergoing One-Dimensional Morphing. *Journal of intelligent material systems and structures* **2010**, *21* (17), 1737−1753.
(44) Rawson, S. D.; Bayram, V.; McDonald, S. A.; Yang, P.; Courtois, L.; Guo, Y.; Xu, J.; Burnett, T. L.; Barg, S.; Withers, P. J. CT Analysis: Distance to Sample Edge Matlab Function. *Zenodo*; CERN, 2021; DOI: 10.5281/zenodo.4749210 (accessed 2021-05-27).
(45) Rawson, S. D.; Bayram, V.; McDonald, S. A.; Yang, P.; Courtois, L.; Guo, Y.; Xu, J.; Burnett, T. L.; Barg, S.; Withers, P. J. CT Analysis: Spacing between Lamellar Features. *Zenodo*; CERN, 2021; DOI: 10.5281/zenodo.4749274 (accessed 2021-05-27).

https://doi.org/10.1021/acsnano.1c04538
ACS Nano 2022, 16, 1896−1908